Signal Formation and Recognition with the Liquid Xenon Compton Telescope LXeGRIT

U.G. Oberlack[a], E. Aprile[b], A. Curioni[b], K.L. Giboni[b],
M. Kobayashi[b] *and same author list as in calibration paper?*

[a]*Department of Physics & Astronomy, Rice University, Houston, TX, USA*
[b]*Columbia Astrophysics Laboratory, Columbia University, New York, NY, USA*

Abstract

LXeGRIT is a Compton telescope for MeV gamma-ray astronomy, based on a liquid xenon time projection chamber. This homogeneous detector measures the energy deposits and the 3D positions of all gamma-ray interactions within its sensitive volume and images sources like a traditional double-scatter Compton telescope. The charge signals on X-/Y-induction wires and on four separate anodes are recorded as a function of electron drift time. The analysis procedure extracts the charge signals from the data, measures the energy deposits with high accuracy through anode waveform fitting, matches wire and anode signals, and distinguishes between γ-ray, charged-particle, and noise events. We discuss the performance of signal recognition with LXeGRIT, and compare it with expectations based on detector properties and simulations.

---

1 Introduction

In this paper, we discuss the performance of a signal recognition technique for a liquid xenon time projection chamber (LXeTPC), which is the centerpiece of the first balloon-borne Compton telescope with this technology, LXeGRIT. Fig. 1 shows a schematic of the LXeTPC. It consists of a $20 \times 20 \times 7$ cm^3 sensitive volume filled with high-purity, liquified xenon, which is an efficient scintillation and ionization medium. The fast scintillation light, viewed by four UV-sensitive photomuliplier tubes (PMTs) from below, provides the trigger. Electrons are drifted in a 1 kV/cm field, applied between a solid ceramics cathode and a wire mesh used as a Frisch grid. In the collection region below, two orthogonal wire layers sense the induction signals of the drifting electrons, providing X-Y localization. Each charge cloud is collected on one of four separate anodes, made of wire meshes, which accurately measure the energy

Preprint submitted to Elsevier Science *Draft version: 9 March 2003 20:29 h*

deposits of individual γ-ray interactions. Z-coordinates are derived from the drift time with respect to the light trigger and from the known drift velocity of $\sim$ 2 mm/μs. The TPC is enclosed in a cylindrical vessel, containing the liquid at an operating pressure of 1.5 – 2.3 atm, and is thermally insulated by a vacuum cryostat, encompassing the PMTs, to maintain a temperature of $-90°$ to $-95°$ between periods of cooling with liquid nitrogen. For details on the spectral and imaging performance, and the 1999 LXeGRIT in-flight set-up, we refer the reader to [1,2]. We discuss the charge signals in greater detail in section 2.

Imaging of γ-rays with the LXeTPC requires multiple (at least 2) interactions, where the first interaction is a Compton scattering and the γ-ray energy is fully contained in the detector. The analysis of γ-ray data consists of several steps, outlined in section 3: event selections (3.1), identification of corresponding X- and Y-wire signals (3.2), identification of anode signals and an accurate determination of the pulse heights by fitting (3.3), matching of wire / anode signals and refitting of the anode waveforms where necessary (3.4), and reconstructing the time sequence of the signals. At this point, many improper event types (and therefore background) have been rejected. Imaging proceeds with techniques as for classical double-scatter Compton telescopes, i.e., by determination of the scatter direction between first and second interaction, and by the measurement of the Compton scatter angle φ, based on measured energy deposits and Compton kinematics:

$$\cos\varphi = 1 - \frac{m_0\, c^2}{E_\gamma - E_1} + \frac{m_0\, c^2}{E_\gamma} \tag{1}$$

where $m_0\, c^2 = 511$ keV is the electron rest mass, E_γ the γ-ray energy, and E_1 the energy deposit in the first interaction. Scatter direction and scatter angle define a circle on the sky (a ring, including measurement uncertainties), from which the γ-ray has originated. Many photons from the same source result in intersecting ‘event circles’, with varying radii, defining the source position. In fact, additional information is available from the known probability density for scatter angles within the telescope for a given source location, leading to more powerful imaging techniques. Moreover, a phenomenological or physical model of the remaining background is required. Both topics, however, are beyond the scope of this paper, and we refer the reader to various examples with COMPTEL data [3–5].

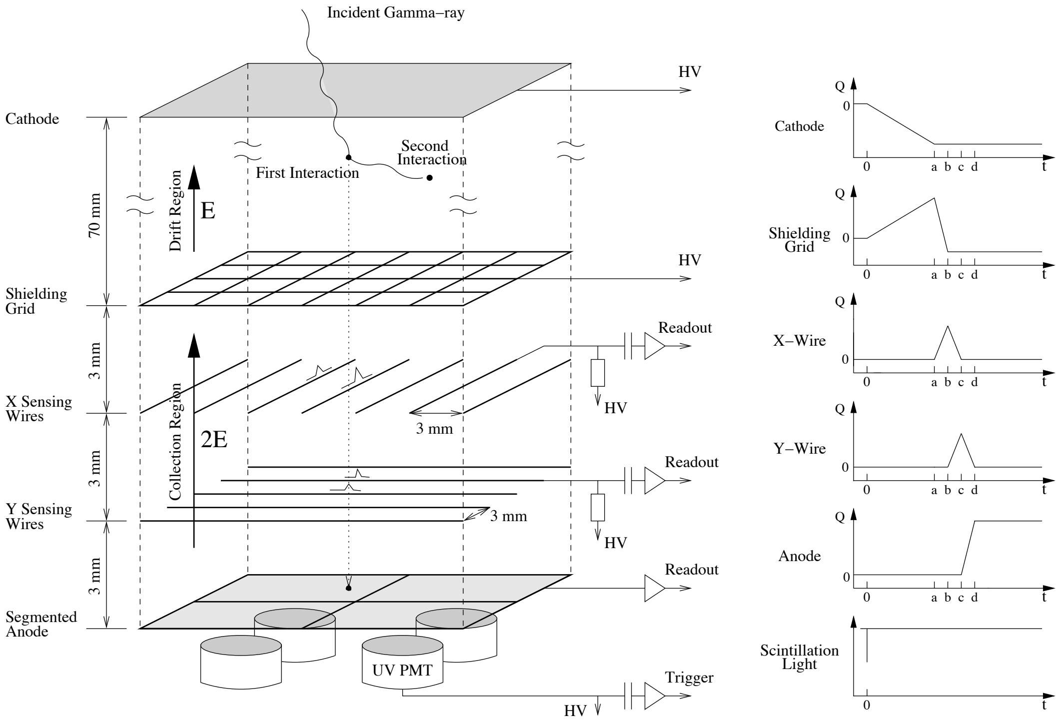

Fig. 1. Schematic of the LXeTPC read-out structure with corresponding light trigger and charge signals.

2 Charge signals in the LXeTPC

Fig. 1 shows a schematic of the read-out structure on the left side and the corresponding charge signals, with inverted signs, observed on the various electrodes on the right side, together with the light trigger signal in the bottom right inlet. A 7 cm drift region (not to scale) is bounded by a ceramics cathode on top and the shielding grid below. A γ-ray interaction in the drift region triggers the data acquisition (DAQ) system through a fast scintillation signal (time 0) and generates a charge cloud, which can be considered point-like, given its small extent of ~ 0.5 mm for a 1 MeV energy deposit, and negligible diffusion in the liquid. The electron cloud drifts in a uniform field of 1 kV/cm at a speed of ~ 2 mm/μs, inducing immediate induction signals on shielding grid and cathode, which are, however, not read out. The signals from the drifting ions, orders of magnitude slower, are not observed and omitted in the graph. The electric field is doubled in the collection region below the grid, to focus the drifting electrons through the mesh and a structure of 2×62 X- and Y-wires, with a pitch of 3 mm. Grid, wire layers, and anodes are all separated by 3 mm from each other. No signal is seen before the charge cloud passes the grid at time 'a'. The drifting electrons subsequently induce a linearly increasing charge on the X-wire until they reach the X-plane at time 'b'. The X-signal decreases at the same rate back to zero, as the charge moves toward the Y-wire plane, which it reaches at time 'c'. The rise and fall times

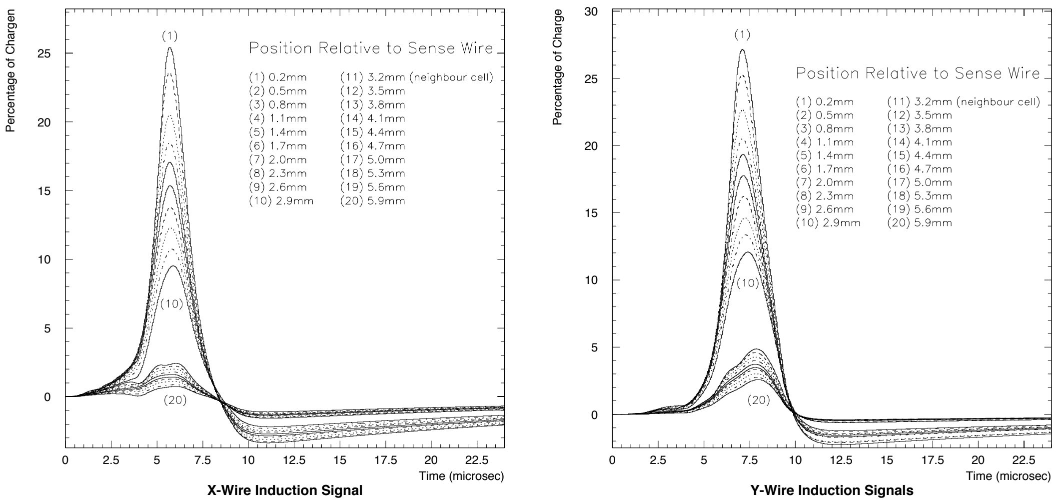

Fig. 2. Simulated induction signals on X- and Y-wires for different distances from the sensing wire. Graphs 1–10 are for positions between one wire and its neighboring wire, while graphs 11–20 are for positions beyond the neighboring wire.

of the triangular wire signals are therefore given by the drift time between the grid, wire, and anode planes, respectively. The anode signal starts to rise only at time 'c', until the charge is collected at time 'd'. The pulse height of this "step" is proportional to the energy deposit.

The read-out electronics is described in [6], and recent upgrades in the DAQ system are discussed in [7]. Here, we only summarize briefly. Wire and anode signals are fed into low-noise, charge-sensitive preamplifiers, and the entire waveforms are digitized with Flash ADCs and recorded over a time span of 51.2 μs, at a sampling rate of 5 MHz. The stored waveforms are read out by a microprocessor, if the event fulfills various online selection criteria. At least a minimum anode threshold crossing is usually required. Additionally, a minimum and maximum number of threshold crossings on the wires can be required ('minmax' criterion), and the anode signals can be tested for saturation. In flight, only wire signals above pre-set thresholds are read out ('reduced read-out mode'), to accelerate data acquisition, and to reduce the amount of data to be stored or transmitted. For noise evaluation, the DAQ system still acquires every 50$^{\text{th}}$ event with all wire and anode waveforms. In 'full read-out mode', every accepted event is recorded in its entirety.

Wire and anode signal shapes in the LXeTPC were simulated to optimize the electronics design [8] and electric potential settings. The simulation uses the GARFIELD code [9], a two-dimensional drift-chamber simulation program, to compute the electrostatic field distribution as well as the weighting potentials for the read-out structure. This is used as a basis to compute the signal shapes, including rise and decay times of the preamplifier circuit. The simulation assumes a wire diameter of 100 μm, an electron drift velocity that increases slightly from 2.05 mm/us at 1 kV/cm to 2.25 mm/μs at 2 kV/cm, as well as

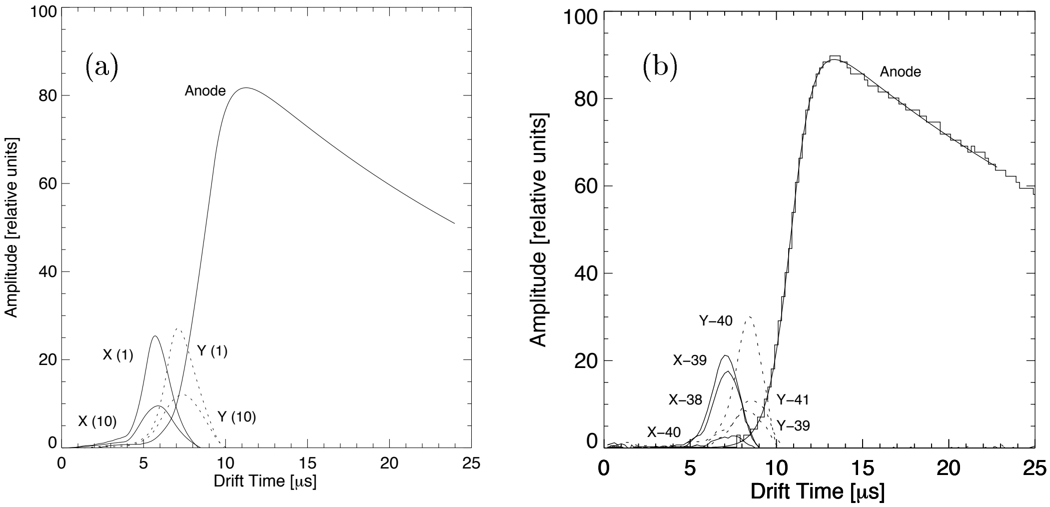

Fig. 3. (a) Simulated collection signal on an anode compared to induction signals at a perpendicular distance of 0.2 mm (1) and 2.9 mm (10). [8] (b) Measured anode and wire signals as a function of drift time for a γ-ray energy deposit of 1.8 MeV. A fit to the anode signal is overplotted. The amplitudes of anode and wire signals are gain-corrected and normalized to the fitted amplitude of the anode.

electronic shaping with a rise time of 1.5 μs (10% – 90%) and an exponential decay time of 25 μs. Fig. 2 shows the induced signals on X- and Y-wires for various lateral distances of the charge cloud with respect to the sensing wire. The charge is always seen on at least the two neighboring wires, with a relative weighting depending on its location inbetween. This provides, in principle, a means for improving position resolution to better than 3 mm/$\sqrt{12}$ rms, the value for independent signals on wires with a pitch of 3 mm. This is hampered, however, by the limited signal/noise ratio for small wire signals, as well as by the applied focusing of the electron clouds, which aims at reducing charge collection on shielding grid and sensing wires. Wires in neighboring "cells" see a much reduced signal, which is usually not measured for signals of $\lesssim$ 1 MeV, but becomes apparent in the 1.8 MeV data. In Fig. 3a, the corresponding anode signals are overlaid with the wire signals. Electronic shaping on the anodes was modeled with 2.0 μs rise time and 50 μs decay time. Fig. 3b shows *measured* anode and wire signals as a function of drift time for a γ-ray energy deposit of 1.8 MeV, with a fit to the anode signal superimposed. The amplitudes of anode and wire signals are gain-corrected and normalized to the fitted amplitude of the anode. Three wires show signals on each view. The signal of the middle wire is plotted in black, the others in gray. At lower energies, the number of wires with a signal belonging to the same interaction decreases, whereas at higher energies, the extent of the electron charge cloud becomes comparable to the spatial resolution of the chamber. The maximum amplitudes of the wire signals are at a level of 20% – 30% of the fitted anode amplitude (which is somewhat larger than the maximum of the anode waveform, due to signal shaping). The data resemble closely the simulated signals.

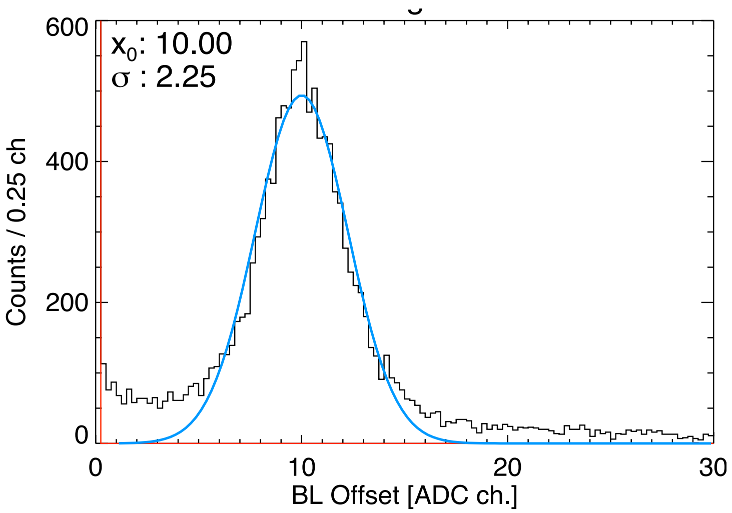

Fig. 4. Histogram of anode baselines, from a time stretch during the 2000 balloon flight.

3 The signal recognition and fitting procedure

Fig. 5 shows the FADC pulse height signals on all wires and active anodes as a function of drift time for an 1836 keV γ-ray event with four interactions (three Compton scatters and one photo-absorption). The requirement of low noise is particularly apparent for the smallest reconstructed step, which corresponds to an energy deposit of only $\sim$ 100 keV. The figure illustrates several steps in the process of signal recognition and event reconstruction, which are presented in the following paragraphs.

3.1 Event selections

The identification of good γ-ray events is achieved through several steps throughout the analysis procedure. Initial selections are as follows:

(1) Events for which the anode baseline, measured in the first 20 samples, is outside a specified range around a nominal baseline value are rejected, as shown in the baseline distribution of Fig. 4. Also rejected are events for which the baseline value of the first 10 samples differs by more than the same preset value from the baseline value of the subsequent 10 samples. Such events are due to a signal in the collection region, to pile-up with a previous signal that did not trigger the detector, or to noise. Moreover, events with a digitized anode baseline of zero are rejected, since the full signal amplitude cannot be determined in such cases. This can happen if a preceding event, e.g., a cosmic ray, deposited a large amount of energy in the chamber, resulting in an undershoot of the signal waveform before

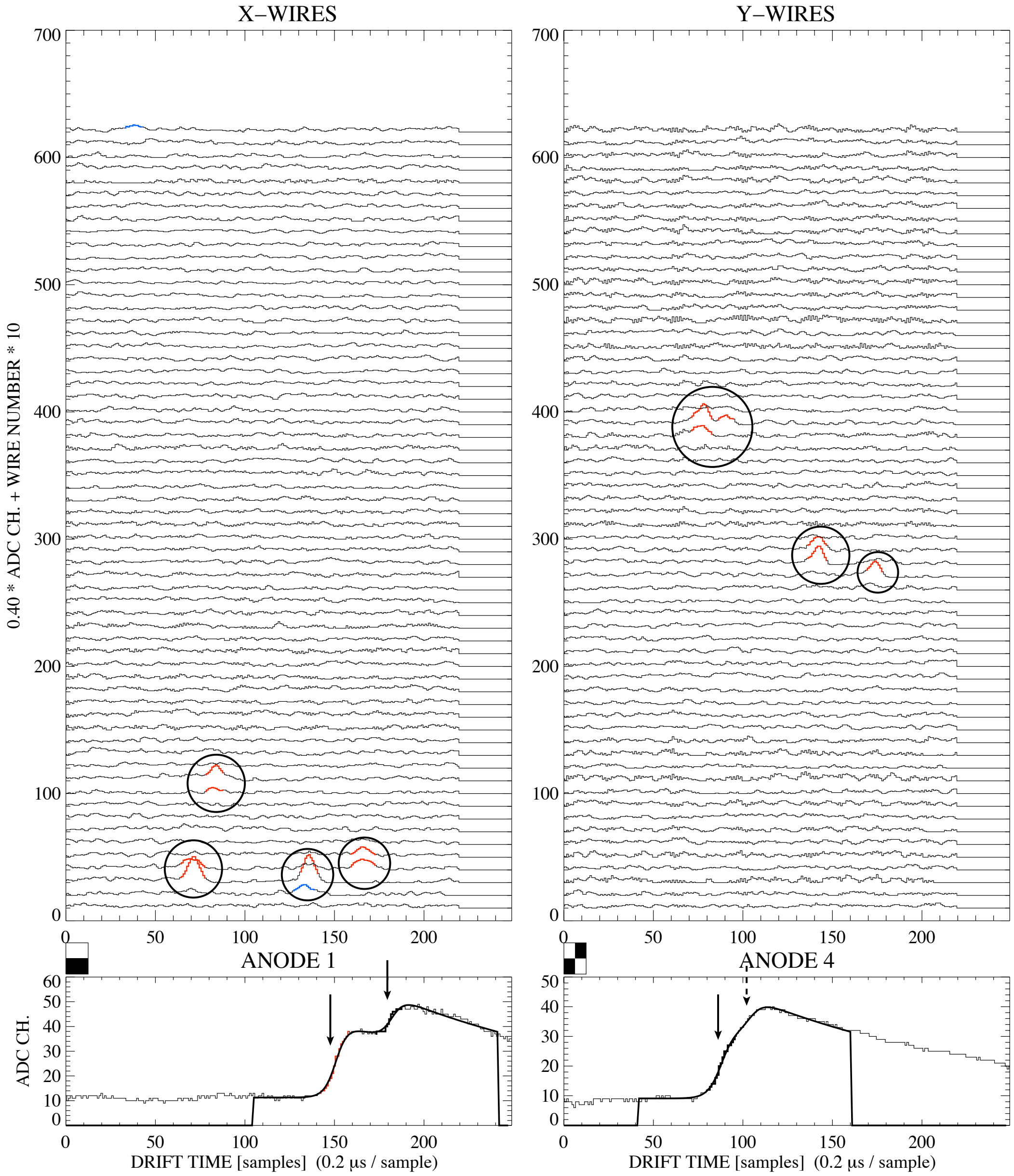

Fig. 5. Digitized waveforms on wires and active anodes as a function of drift time in FADC samples, for an ^{88}Y 1836 keV γ-ray event with 4 interactions. The upper panels show all wire waveforms, in scaled units of ADC channels, each separated by an offset. Matched wire signals are indicated by circles, and only their corresponding anodes are shown. The wire-anode correspondence is indicated by the dark fields at the top left corner of each anode display. The solid arrows mark three steps found by the anode signal algorithm, and the dashed arrow marks an additional step, included in the fit (smooth solid line) after signal recognition on the wires.

the nominal baseline is restored.

Some events have signals at unphysically high drift time, e.g., due to the coincidence of a γ-ray that did not trigger the DAQ itself with a preceding γ-ray (pile-up) or noise trigger. However, we do not reject such events at

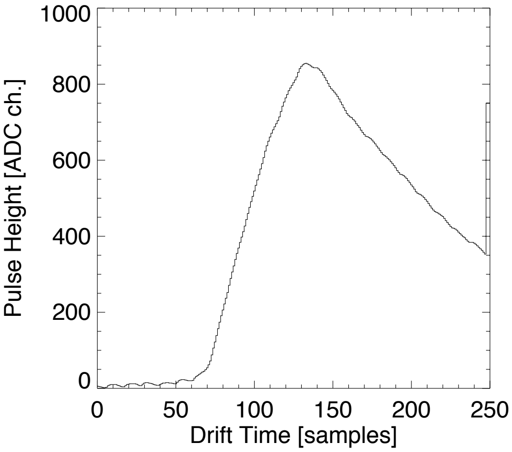

Fig. 6. Cosmic ray track as seen on an anode.

this point yet, since it is practical to use them in a drift histogram, to estimate the total contamination fraction of the sample with such chance coincidences. Note that the LXeTPC electronics is capable of rejecting pile-up events online. Yet, due to the limited light collection efficiency and its non-uniformity in the current detector design [10], a significant fraction of low-energy events can escape the online pile-up rejection. Pile-up becomes significant at rates of a few kHz, e.g., at 5 kHz, about 20% pile-up is expected within the drift time of $\sim 40\ \mu$s.

(2) Charged particles are rejected by amplitude, if any of the anodes is saturated, or by signal rise time. If the slope of the waveform remains positive for more than a specified number of samples, the event is considered a charged-particle track. Empirically, this number has been optimized to 42 samples, while a γ-ray signal usually rises over no more than ~ 25 samples. This charged-particle rejection is still relaxed, not to throw away multiple-step events with small Z-separation on the same anode, which could also generate a positive signal slope in a wide band. Fig. 6 shows an example of a cosmic-ray track on an anode.

Cross-check rise times of high-energy γ-rays.

3.2 Wire signals

Wire signals are found above preset or updated thresholds. Their drift time (t_{d}) values are determined by an amplitude-weighted average within ±5 samples around the position of the signal maximum. The signal amplitude is taken as the maximum value above baseline and corrected for small gain differences in the preamplifiers with calibration factors derived from test pulse data. The signal width is defined as the width in which the signal is above half the amplitude value, approximating the true FWHM. Fig. 7 shows a histogram of wire signal widths. The data are from irradiation of the LXeTPC with a ^{22}Na source at a distance of about 40 cm on top of the vessel. The distribution is

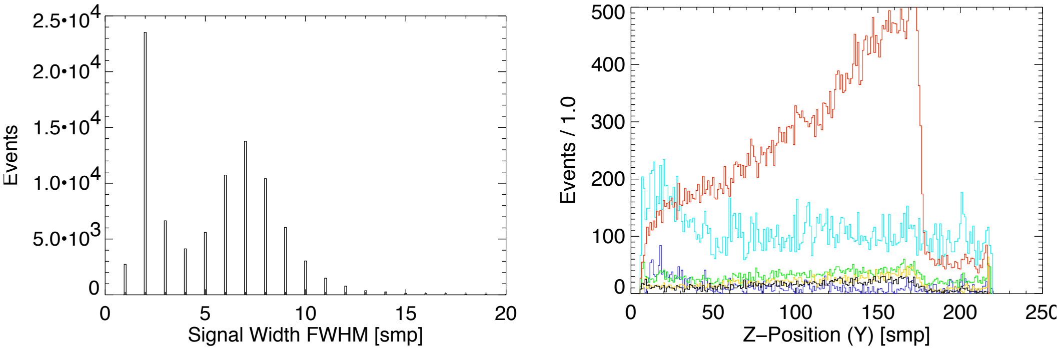

Fig. 7. Left panel: Width of (Y) wire signals recognized above threshold. Right panel: Z-distributions of wire signals for different signal widths. *Note: Label right panel, show only 2 graphs.*

bimodal, with the true signals centered around a width of about 7 samples with a spread of 4.2 samples FWHM. The expected signal width is about the same as the drift time between X- and Y-wires (6.3 samples). The second population of wire signals clusters around 2 samples, with a spread of 1.4 samples FWHM, and consists mainly of noise hits, as can be seen from the drift time distribution on the right panel of Fig. 7. The figure shows separate curves for signals with a width of 4–11 samples and for signals with a width of 3 samples or less. The true signal distribution shows a monotonically increasing distribution with drift time, as expected for attenuating γ-rays from a 511 keV source on top of the chamber, with a sharp edge at the maximum drift time, corresponding to the cathode position. The noise distribution, on the other hand, is relatively flat, and extends without drop beyond the maximum drift time. In fact, the distribution is somewhat enhanced at the beginning of data sampling, probably due to enhanced digital noise. To reduce the number of noise hits, we require valid wire signals to have a width of at least 3 or 4 samples and a maximum width of 16 or larger. Visual inspection shows that broad signals are often due to charge collection on the wires, which occurs preferentially near the edge of the sensitive volume where the electric field becomes less uniform. Other effects resulting in wide wire signals are the occurrence of two unresolved close interactions, high-energy events that saturate the 8-bit dynamic range, or low-frequency noise. Optionally, the entire event can be rejected if a wide wire signal is found, in which case the acceptable width is relaxed to ~ 30 samples.

Optimum wire thresholds can be derived from test pulse or test trigger data, but are usually determined from the data directly, using events with all wire waveforms recorded. This is the case for every event in full read-out mode, and every 50th event in reduced read-out mode. Since charged-particle tracks are rejected in the initial step of the analysis, the remaining (γ-ray) signals only affect a small fraction of all wire samples, and provide hence a continuous

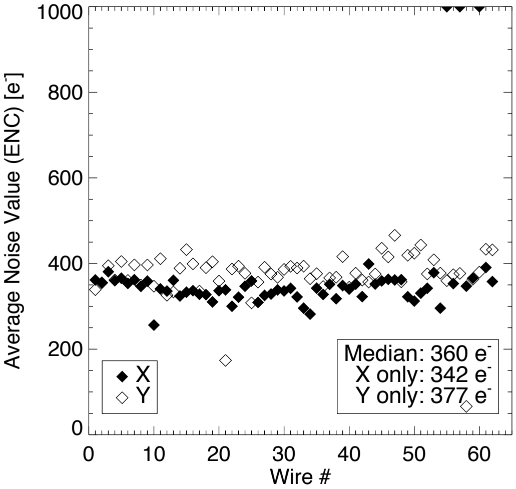

Fig. 8. Wire noise in units of equivalent noise charge (ENC).

monitoring of the noise level on each wire. The analysis procedure provides a user-selectable scale factor α_{w}, by which the noise value on each wire is multiplied to derive individual thresholds. Fig. 8 shows that most of the wires have similar noise values of $\sim$ 360 e^- equivalent noise charge (ENC), computed as mean absolute deviation over 220 samples. Data from an experiment on April 3–4, 2000, used in the following to discuss the impact of noise on anodes and wires, show slightly enhanced noise on a few Y-wires. We use the mean absolute deviation (mdev) rather than the standard deviation (rms) to measure the noise, because it is more robust against high-amplitude 'outlier points' from true wire signals. Since the noise distribution is usually Gaussian in shape, rms = 1.25 mdev, and therefore ENC $\approx$ 450 e^- rms. Particularly noisy wires can be excluded from consideration.

FIG: Wire (and anode?) baselines as a function of time? Or histogram of wire baseline deviations?

Once all wire signals are found, signals from up to three neighboring wires are combined to one signal if their time coincides to within ±2.5 samples (0.5 μs). This signal "collection" is necessary because even an ideal point charge distributes its signal over at least two wires, as was shown in Section 2. The algorithm starts with the largest signals, searching for signals on the two neighboring wires, and continues through all remaining wire signals on both views. The amplitudes of the signals in X- and Y-clusters are added and the interaction locations in X or Y, and in t_{d}, are weighted by amplitude. In addition, the focusing effect of the electrical field in the collection region on the X/Y positions is corrected as follows (for X):

$$X = \langle X \rangle_w \, f + \langle X \rangle \, (1 - f)$$

where $\langle X \rangle_w = \sum_i A_i \, X_i / \sum_j A_j$ is the amplitude-weighted position, $\langle X \rangle =$

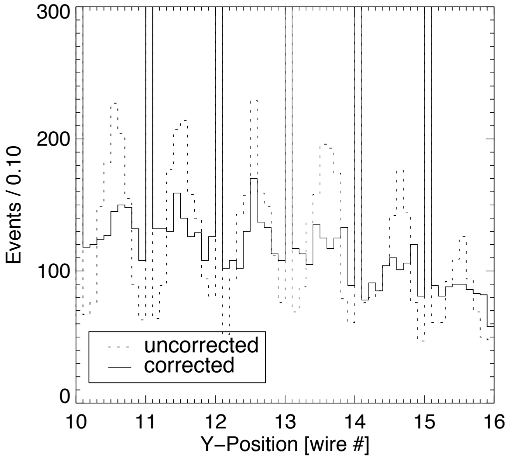

Fig. 9. Zoom on interaction locations measured on Y-wires 10–16. The dotted line indicates the positions based on an amplitude-weighted average, and the solid line shows the corrected positions, accounting for the focusing effect of the enhanced field in the collection region. The peaks at integer wire numbers are due to single-wire signals, which are unaffected by the correction.

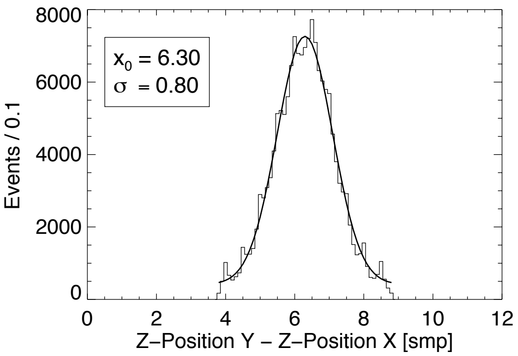

Fig. 10. Distribution of drift time differences between matched wire signals in Y and X. The width of 0.8 samples (1σ) corresponds to a measurement accuracy of 160 ns in drift time or 0.32 mm in Z.

$\sum_i X_i/N$ is the average position, and $f = E_{\text{coll}}/E_{\text{drift}} = 2$ is the focusing factor, i.e., the ratio of electric field strengths in collection and drift region. Fig. 9 shows the correcting effect, making the position distribution significantly more uniform. The number of collected signals increases slowly with energy, from typically a single wire near the lower enery threshold to up to three wire signals at higher energies, as the weaker signals on adjacent wires emerge from the noise.

In the next step, the combined induction signals on the X- and Y-view are matched in drift time (marked with circles in Fig. 5), again within a narrow window of ±2.5 samples, after subtraction of the drift time offset between the X- and Y-wire planes of the measured mean value of 6.3 samples (1.26 μs). This value corresponds to a drift velocity of 2.4 ± 0.1 mm/μs in the collection region, at a field of 2 kV/cm. Fig. 10 shows the distribution in drift time dif-

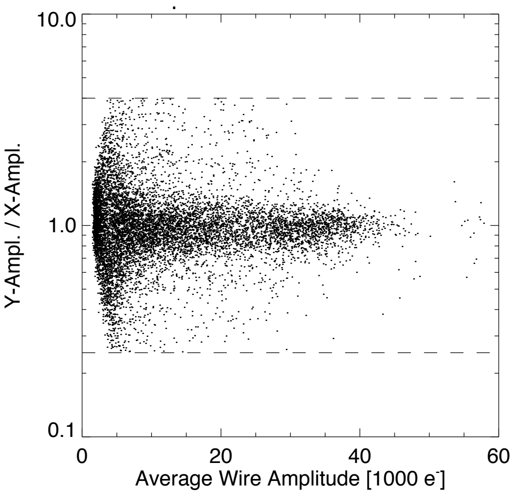

Fig. 11. Scatter plot of the amplitude ratio Y/X versus the mean value of X- and Y-amplitudes, expressed in charge units of 1000 e^-. The dashed lines show the cuts applied during the analysis. Notice that the Y-axis is logarithmic.

ference between Y- and X-signals. It has a width of typically $\sigma = 0.8$ samples, or 160 ns, which narrows to the theoretical limit of $\sim$ 140 ns for the sampling time of 200 ns if sufficiently large wire signals are selected. The acceptance window for X/Y-matching corresponds therefore to about $\pm 3\sigma$. In addition, the signal amplitudes are required to be similar within a user-selectable factor, usually set to a value of 4. At large amplitudes, the correspondence between matching wire signals is in fact significantly better than this, as can be seen in Fig. 11, where the amplitude ratio Y/X is plotted versus the mean value of X- and Y-amplitudes. At small charge signals ($\lesssim$ 6000 e^-, corresponding to $\lesssim$ 300 keV), however, one of two wire signals can be missed and the energy resolution of the wire signals degrades, such that X- and Y-amplitudes of matching signals can differ significantly. At very low amplitudes, the scatter in amplitude ratio is reduced again, due to the minimum amplitude required by the thresholds.

If the match by drift time is not unique, the better match by amplitude is chosen. The requirement on the drift time match within a 5 samples wide window reduces the noise from chance coincidences by a factor of $\sim 220/5 = 44$, where 220 is the number of samples in which a wire signal is searched. Occasionally occurring noise spikes, which affect all wire signals, are efficienctly rejected since they do not show the required drift time offset. Unless the wire threshold parameter $\alpha_{\rm w}$ is set very low, the tight drift time selection is mostly sufficient to find a unique match.

Fig. 12 illustrates to which extent the LXeTPC wire structure can separate individual interactions. Noting that X and Y spatial resolution are identical, the left panel shows the Y- versus Z-separation between the interactions in events where two matched X/Y wire signals were recognized, independent

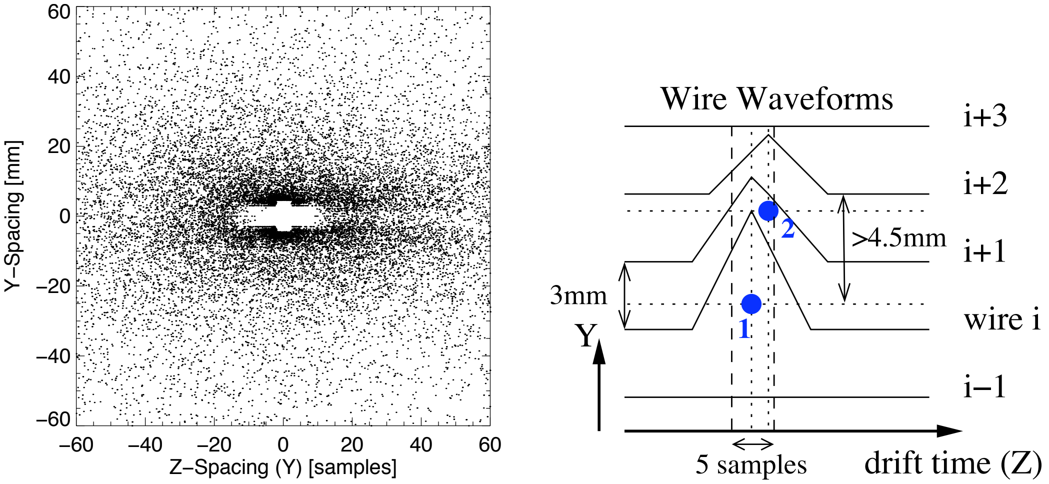

Fig. 12. Left panel: Y- and Z-separation of events with two X/Y-matching wire signals, without consideration of anode signals, for ^{88}Y data. Right panel: Schematic of wire signal waveforms versus Y and Z. Two interactions, with charge clouds indicated by filled circles, within ±2.5 samples drift time can only be separated if they occur in separate 'cells' of wire pairs on each view.

of the anode signal. The physical distribution of separations should fall off exponentially, with a peak at zero. Two interactions that fall within the same drift time window of ±2.5 samples, i.e., $|\Delta Z| \lesssim 1$ mm, are only separated if they occur in separate 'cells' of wire pairs in both X and Y views. If they are identified as separate interactions, their assigned coordinates will have a separation of at least 4.5 mm, i.e. 1.5 times the pitch. The reason is illustrated in the right panel, for two minimum separable interactions: Wire $i+1$ sees signals from both charge clouds. If both signals are sufficiently close in drift time, and/or the charge clouds are sufficiently close to this wire, it will have the largest amplitude of the three wires, and would be combined into one signal ('confusion'). If wire i has the largest amplitude, wire $i+2$ is recognized as a separate interaction, and the coordinates will result from the weighted average of i and $i+1$ for interaction 1 and the coordinate of wire $i+2$ for interaction 2. Hence, the minimum reconstructed Y separation is 1.5 times the wire pitch.

If both interactions occur within the same cell (on either view), a minimum separation in Z of about the signal width is required, we find ~ 8 samples (3.2 mm). Electronic undershoot somewhat worsens the situation, depending on the amplitude ratio of the signals, and a significant effect can be seen up to ~ 15 samples (10 mm). If the energy deposit at lower drift time is much larger than the energy deposit at higher drift time, the effect can extend to even farer separations, as can be seen as a weak effect on the right half of the scatter plot. These misses of close interactions directly affect the multiplicity of detected interactions, as will be discussed in section 4.

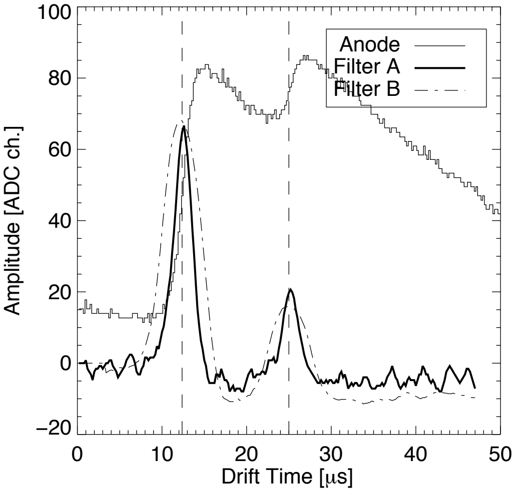

Fig. 13. Anode signal recognition, here for a 2-step event, applying two filters. Filter A determines the step position precisely, while filter B measures the signal amplitude. Both values become start parameters for subsequent waveform fitting.

3.3 Anode signals

Recognition of anode signals, shown in Fig. 13, uses a filter 'A' which computes for each FADC sample i a smoothed first derivative, by subtracting the samples $[i-5, i-1]$ from the samples $[i+1, i+5]$. A step is found if the filtered waveform crosses a preset threshold and remains above for at least 5 samples. Filter 'B' subtracts the samples $[i-16, i-9]$ from the samples $[i+9, i+16]$, and is usually used for an initial estimate of the step height only. However, for data under rather noisy conditions, one can additionally require that both filters be above a preset threshold. Strong *negative* slopes that follow within 6 samples of a positive threshold crossing, are associated with digital noise, and the affected anode samples are excluded from fitting. The mean time difference between X-wire signal and anode signal is about 17 samples, due to the drift time difference and signal shaping on the anodes, thus X signals will be missed for early anode signals, resulting in incomplete events. These events, which correspond mainly to interactions within the collection region, are therefore rejected. The requirement of a reliable baseline estimate for the determination of the step height, led us to keep a more conservative cut, discarding all events with anode signals within the first 20 samples. This corresponds to a fiducial volume cut of the lowest ~ 4 mm in Z.

The energy deposits in individual interactions are derived from a fit of the anode signal, plotted as smooth line on top of the anode waveforms in Fig. 3b and 5. The fit function consists of one or multiple steps described by Fermi-Dirac thresholds, an exponential decline, and a flat baseline. For a one-step

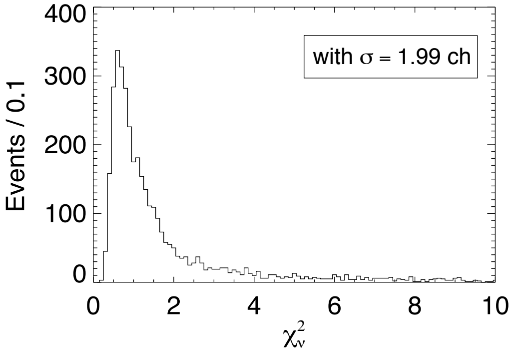

Fig. 14. Reduced χ^2_ν-distribution of 1-step fits for anode 1 and ^{88}Y data (102 degrees of freedom).
Note: Overplot χ^2_ν for the two photopeaks, to show energy dependence?

anode signal, the function is defined as follows:

$$f_1(t) = a_0 \cdot \left(1 - \frac{1}{1 + \exp\{a_2\,(t - a_1)\}}\right) \cdot \exp\{-a_3\,(t - a_1)\} + a_4 \qquad (2)$$

where a_0 is the signal amplitude, a_1 is the step position measured at about half height of the signal, a_2^{-1} describes the signal rise time, a_3^{-1} is the exponential decay time resulting from RC shaping in the preamplifier, and a_4 is the baseline value. For n steps, the formula expands to a function with $2\,n + 3$ parameters, since rise time, decay time, and baseline are the same for all steps. The rise time is kept fixed at predetermined values, which vary for the four anodes due to differences in signal shaping, with values a_2^{-1} of 3.31, 3.36, 3.38, and 3.80 samples, respectively.[1] The exponential decay time is also fixed, at 135 samples. The baseline parameter a_4 is determined for each event in a separate step before the waveform fit, to increase fit stability and to prohibit undesired trade-offs between signal and baseline determination for noisy signals. a_4 is set to the average over a 30 samples wide window at $[-45, -15]$ samples before the initial estimate of the step position. The fit range is restricted to $[-45, +60]$ samples around the initial position estimate, to make the fit less susceptible to low frequency noise, and to reduce systematics from the simplified description of the signal decline by a single exponential. In case of multiple steps, the fit range is extended to the first step position -45 samples and the last step position $+60$ samples.

Fig. 14 shows the reduced χ^2_ν-distribution for fits of 1-step events on anode 1, for ^{88}Y data. We applied the standard deviation within 220 FADC samples (2.0 ch.), determined from ‘empty’ anode waveforms, as error estimate on each sample value. The distribution peaks at 0.6 and exhibits an extended tail. It is therefore quite different from a reduced χ^2_ν distribution with 102 degrees

---

[1] This corresponds to (10% to 90%) risetime values of 2.9, 3.0, 3.0, and 3.33 μs.

of freedom. This indicates that the noise description is not accurate for this purpose, and, more importantly, that the fit is not satisfactory for all events. The shape of the anode signals is not completely described by the analytical function, and the deviations become more evident for large signals. Therefore, we also see an increase of the minimum χ^2-value with increasing energy. From such dependencies and by visual inspection of fits, an empirical cut-off value for acceptable fits can be determined. Note that the fit quality is independent of drift time. If the fit fails, the event is rejected. A calibration with radioactive sources ultimately translates the amplitude of each step into the interaction energy deposit [1].

3.4 Matching of wire and anode signals

In the next step, the identified and matched X- and Y-signals are matched with the recognized anode signals, based on drift time and a correspondence of (X, Y)-position and anode location. If all n signals match, the event is stored as n-interaction event. If more anode signals are found, all anode signals and all matching wire signals are stored, and the event is labeled correspondingly. If more wire signals are found, we attempt to refit the corresponding anodes with the additional steps, unless they are separated from other signals on the same anode by less than 10 samples in drift time. The anode step positions are restricted to a range of ±4.5 samples around the Y-wire position, plus an empirical drift time offset of 11–13 samples, depending on the anode. If the anode fit is sufficiently improved and the newly fitted anode steps exceed a minimum amplitude, the refit is accepted, and the event is correspondingly flagged. Additional wire signals, for which no anode signal above a preset threshold can be fitted, are considered noise and removed. If there are signals that are too close in drift time to be fitted on the same anode, the event is stored with all wire signals and the matched anode signals, and labeled accordingly. Finally, if the number of matching signals is smaller than both the number of wire signals and the number of anode signals, the event is rejected, as it is assumed that the event reconstruction failed.

Fig. 15 demonstrates the success of the refitting procedure. It shows a comparison of pulseheight spectra of 2-step events with and without refit, for ^{88}Y data. A χ^2_ν cut of 8 was applied. About half of the photopeak events at 1.8 MeV with acceptable χ^2_ν have been refitted, with a similar spectral resolution as events without refit. The refit of the anodes, using the wire signature, enhances the efficiency especially for imaging. Even requiring a minimum spatial separation of 20 mm for an accurate determination of the scatter direction, the refit procedure still adds 24% of selected events to the 898 keV peak, and 42% to the 1836 keV peak.

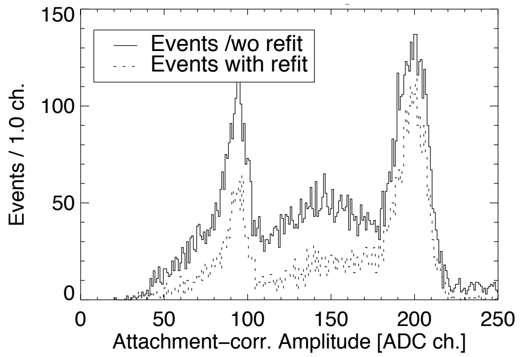

Fig. 15. Pulseheight spectra for events with and without refit, for ^{88}Y data.

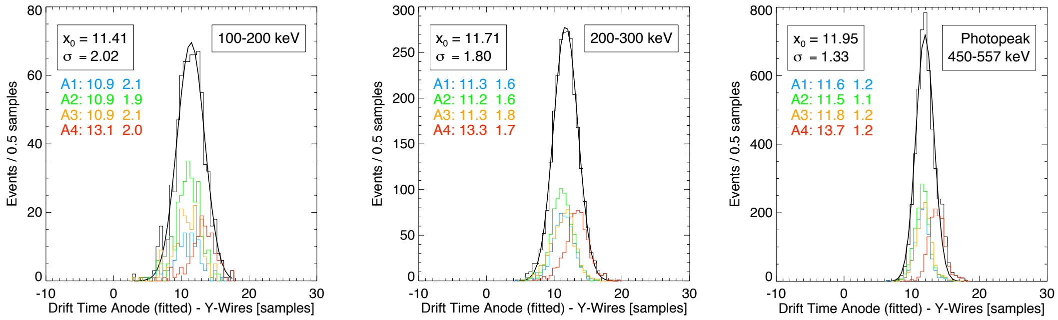

Fig. 16. Distribution of drift time differences between matched wire and anode signals (using the drift time of the Y-wires) in total and for individual anodes, and for three energy bands. From left to right: 100–200 keV, 200–300 keV, and in the 511 keV photopeak of ^{22}Na.

Fig. 16 shows the distribution of the drift time difference between matched wire and anode signals, using the drift time of the Y-wire signals. The peak of the distribution is almost independent of energy, while the width of the distribution increases from a (1σ) width of about 1 sample at 1.8 MeV to 2.2 samples at the lowest energies, between 100 and 200 keV. Based on the electron drift time, the offset would be $3-4$ samples only, since the anode timing is measured at about half rise time. However, the anode signals are shaped with time constants (8.3 and 12.2 samples / 1.7 and 2.4 μs 10%–90% rise time on anodes 1–3 and 4, respectively), which are even larger than the physical signal rise time, shifting the measured signal position to larger drift times. The total signal rise time of 14.7 samples or 2.9 μs (16.7 samples or 3.3 μs on anode 4) would imply a time offset between Y-wires and anodes of $\sim$ 7.5 (8.5) samples. The difference of 3–5 samples to the observed value is due to a delay in the digital electronics, which is also seen between the onset of test pulses on wires and anodes.

Fig 17 shows the absolute value of Z-separation of steps after matching of wire and anode signals. The requirement of a minimum separation of 10 samples for signals on the same anode results in a sharp edge in the distribution. Comparison with Fig. 12 shows that the matching of anode and wire signals

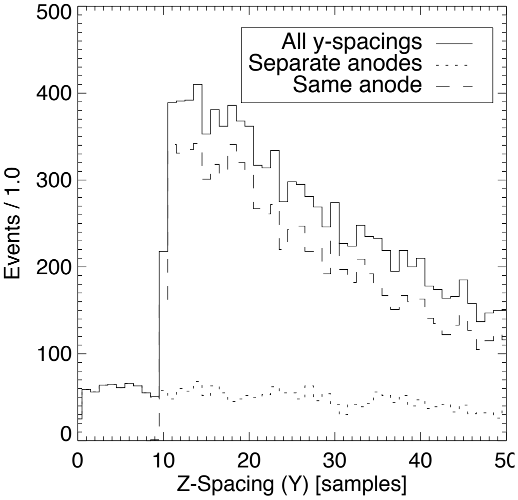

Fig. 17. Z-separation of recognized signals with matching wire and anode signals, for ^{88}Y data.

has a more severe impact on resolving signals close in drift time than the X/Y-wire matching.

4 Efficiency and multiplicity

The overall response function of LXeGRIT is composed of several elements: the efficiency for fully contained Compton scatter events, given by the detector geometry and size, the efficiency of the light trigger system [10,11], online event selections, livetime, and the efficiencies related to signal recognition on wires and anodes. While the complex overall response is the topic of a separate paper[12], we focus here on the combined effect of detector properties, such as spatial resolution and signal/noise ratio, and the effectiveness of the software algorithms, on the ability of the LXeTPC to reconstruct multiple γ-ray interactions. This section discusses three aspects of this combined performance that are particularly relevant to the imaging of γ-rays:

(1) Signal detection efficiency on anodes and wires for small energy deposits, which not only define the effective lower energy threshold of the detector (together with the light-trigger threshold), but, even more importantly, the efficiency with which any γ-ray can be fully imaged and sequenced in time, since the final photoabsorption in xenon typically occurs at an energy below $\sim$ 250 keV, where photoeffect dominates over Compton scattering.
(2) Noise contamination.
(3) Confusion of close signals, limiting the observable multiplicity of interactions in the sensitive volume.

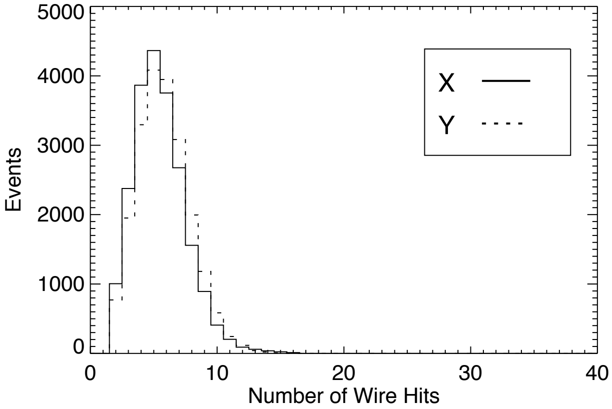

Fig. 18. Number of wire hits as recorded during data acquisition. The upper cut of 16 is without impact, and the minimum cut of 2 hits has only a slight effect.

In assessing efficiency and contamination, selections during data acquisition have to be taken into account. They consist of light trigger settings, anode thresholds, and the requirement of a minimum and maximum number of wire signals above thresholds on each X/Y view ('minmax' criterion). To minimize such online selection effects, we used data from an experiment with a tagged ^{22}Na source [10], thus removing all threshold effects due to the light trigger system of the TPC by using an external trigger. Moreover, the minmax criterion was set to $2-16$, where only the lower cut had a small effect, as is evident from Fig. 18. The most significant online selection is therefore due to the anode thresholds, which were set to 6 ADC channels, corresponding to ~ 130 keV. The online selection criterion requires four consecutive samples to be above threshold on at least one anode, in which case all four anode waveforms are recorded.

4.1 Signal detection efficiency on the anodes

The efficiency with which interactions are identified, depends primarily on the signal/noise ratio. A γ-ray interaction deposits an initial charge of $Q_0 = \Delta E/W_{\mathrm{LXe}}$ in the liquid, which is 6400 e^-/100 keV for $W_{\mathrm{LXe}} = 15.6$ eV. Typically, 83% of this charge escape immediate recombination at the operating field of 1 kV/cm. Attachment of the drifting electrons to electronegative impurities in the xenon amounts to an exponential scale length, in the LXeTPC, of 300–350 μs (about 60–70 cm), which reduces the collected charge by about 5% for an event in the middle of the chamber. The anode measures therefore a charge signal of ~ 5000 e^-/100 keV. Under noise conditions of 900–1100 e^- rms, the detection efficiency for energy deposits of ~ 100 keV, for single anode steps, is near 100%. In most experiments, the online energy threshold for anode signal recognition was set to ~ 130 keV, with its width of ~ 27 keV (1σ) mainly determined by the energy resolution of the detector and electronic noise.

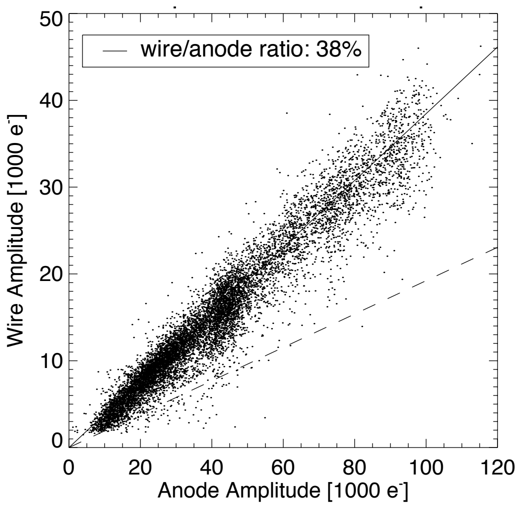

Fig. 19. Scatter plot of wire amplitudes (averaged X- and Y-signal) versus anode amplitudes after gain corrections for a ^{88}Y source.

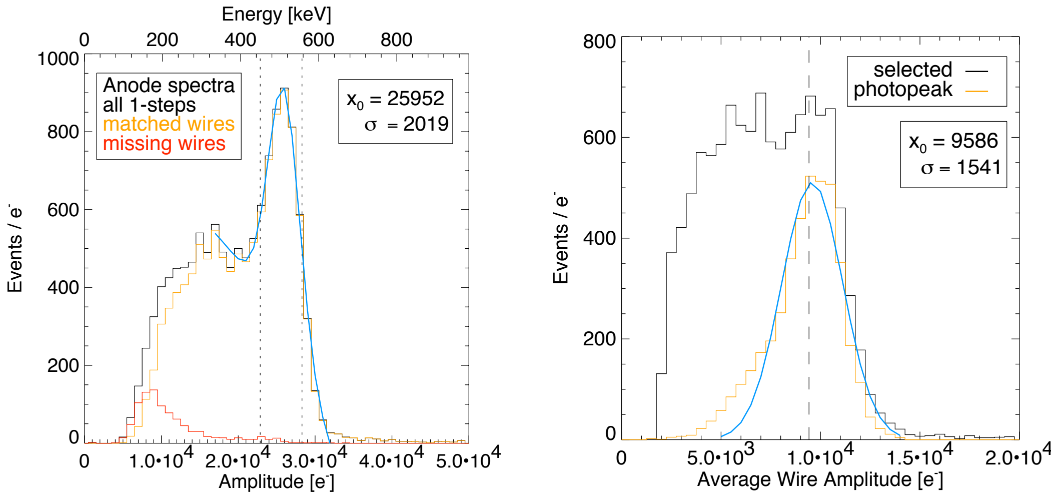

Fig. 20. Pulseheight spectra for a ^{22}Na source. Left panel: anode spectrum with fit of the 511 keV line, and axes labeled in charge and energy units. The black curve shows events with a single anode step irrespective of wire signals. The upper gray curve shows events that have fully matched anode and wire signals, and the lower curve indicates the difference, i.e., events with missing wire signals. Right panel: averaged wire signals, with all events that fall into the photopeak in the anode spectrum overlaid and fitted in the lower curve.

4.2 Signal detection efficiency on the wires

After gain correction with testpulses, charge signals measured on wires and anodes can be compared directly, as shown in Fig. 19 for a ^{88}Y source. A linear fit yields a relative signal strength of about 38% for the collected wire signals, which is consistent with the expectation for two neighboring wire signals (Fig. 3a). The charge spectra on anodes and wires are shown in Fig. 20,

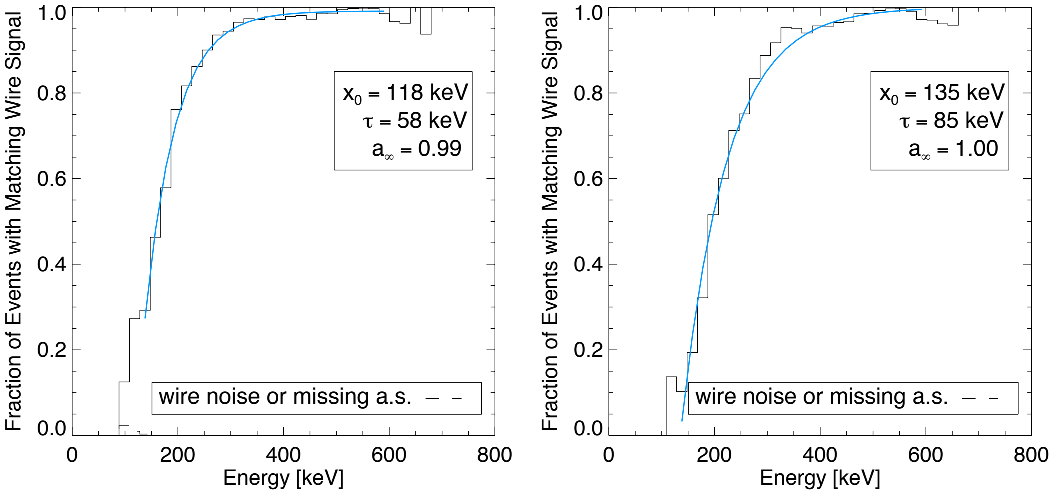

Fig. 21. Ratio of events with one matching anode and (X/Y-matched) wire signal over the sum of all events with one anode signal and one or no matching wire signal. Overplotted (dashed line) is the ratio of events with one wire signal and no anode signal over all events with one wire signal and either one or no matching anode signal. ^{22}Na, anode threshold 5 ch, wire thresholds $\alpha_\mathrm{w} = 4.0$ (left) and 5.0 (right).

with fits of the photopeak events identified on the anodes. At 511 keV, the wire readout is able to resolve the photopeak, even though the spectral resolution is degraded by a factor of ~ 2, and the photopeak shows some low-energy tailing due to partial misses of wire signals on one or both views. The peak value of 9586 e^- collected wire signal at 511 keV corresponds to a charge signal of ~ 940 e^-/100 keV per individual wire, and a signal/noise ratio of 3.1σ at 150 keV, for a typical wire noise value of 450 e^- rms ENC. This is about the typical threshold setting in the analysis (see below).

Depending on the relative location of the charge deposit with respect to the nearest two wires of one view, the charge may be shared asymmetrically, resulting in an effective broadening of the threshold. The amount of broadening due to this effect alone can be estimated from the simulation (Fig. 2), which shows a variation of the signal strength, on the nearest wire, with location of the drifting charges by a factor of about 1.5. A highly asymmetrically shared signal should therefore have a better chance of being detected on the nearest wire than in the symmetrical case.

Given the higher sensitivity of the anodes for single charge signals, the efficiency for finding matching wire signals on X and Y can be estimated as the relative probability of finding a matched wire signal for all events with a single-step anode signal. This conditional probability is given by the ratio of fully matched single site events over all events with a single-step anode signal, irrespective of whether 0 or 1 matching wire signal was found, i.e., the ratio of the upper curve in the left panel of Fig. 20 over the black curve. This ratio

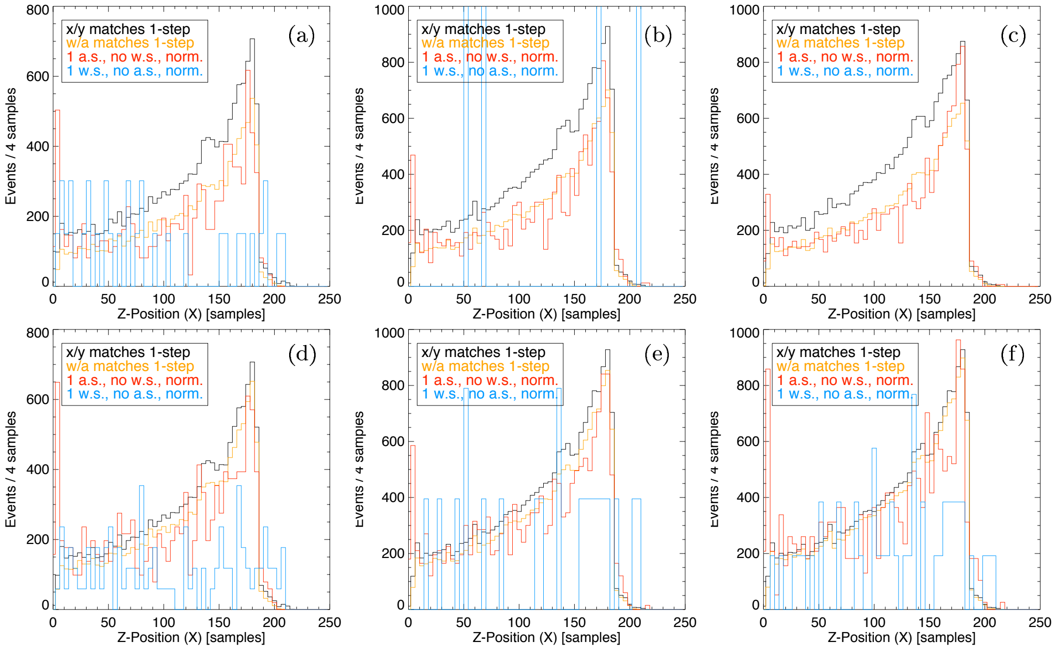

Fig. 22. Drift time distributions of events with exactly one anode/wire matching signal, one anode signal without matching wire signal, and one X/Y-matched wire signal without matching anode signal. For comparison, events with a single X/Y-matched wire signal irrespective of the anode signal is overplotted. ^{22}Na data. (a) – (c): Anode threshold 5 and $\alpha_{\mathrm{w}} = 3.5, 4.0, 5.0$. (d), (e): Anode threshold 6 and $\alpha_{\mathrm{w}} = 3.5, 4.0$. (f): Anode threshold 8 and $\alpha_{\mathrm{w}} = 4.0$.
Note: Remove curve 'x/y matches 1-step'. Change color plots to dashed and dotted lines.

will provide a correct estimate of the wire signal efficiency if:

(1) the efficiency of anode signal recognition is nearly 1 in the energy range of the wire threshold.
(2) there is no appreciable amount of anode noise in that energy range.
(3) wire thresholds are set high enough that chance coincidences of noise hits are insignificant after drift time matching.

Note that statistically independent efficiencies, such as the light trigger efficiency, do not affect this result, as they cancel out in the ratio. Point 1 is fulfilled by pushing the anode threshold to its lowest possible limit. We monitor the noise contributions (points 2 and 3) with drift time histograms: real events can only occur within the physical drift region, and therefore exhibit a sharp cut-off at the maximum drift time t_{max}. Noise events are distributed randomly, and therefore have a flat distribution that extends beyond t_{max}. Fig. 22 shows drift time distributions for three sets of single-hit events: fully matched single-site events, events with one anode signal and no wire signal, and events with one wire signal and no anode signal. In addition, events with a single X/Y-matched wire signal irrespective of the anode signal is overplotted, which in addition to single-site events contains events with two anode signals, for which one X/Y-wire match was missed. Events with one wire signal and no anode signal are identified as noise events, and constitute an upper limit for the wire noise contribution to the fully matched sample. The distributions are shown for various anode and wire threshold settings, exploring the range of valid signals versus contamination with noise.

Changes in noise conditions or threshold settings, both online and offline, affect the location and width of the wire energy threshold, and need to be verified for individual runs. An increase of the individual wire thresholds by 25% is depicted in the right panel of Fig. 21, resulting in a shift of the wire efficiency curve to higher energies. Near optimum settings shown on the left result in energies of 161 keV and 255 keV for 50% and 90% efficiencies. These values are pushed to 193 keV and 304 keV, respectively, for the higher wire thresholds, with estimated uncertainties of ±5 keV.

4.3 Optimum threshold settings on anodes and wires

Maximum efficiency requires lowering the wire thresholds as far as possible, which has to be balanced with increasing noise contamination. In the search for wire signals, about 4500 statistically independent trials (124 wires × 220 samples / 6 samples minimum gap between signals) are made for each event. We tested wire thresholds between 3 and 6 times the measured mean absolute deviation of the noise, corresponding to a range of 2.4 to 4.8σ. For these settings, one expects between 37 and 4×10^{-3} noise hits on all wires per event, in addition to the true signals. X/Y-matching further reduces the expected number of noise hits with fitting drift time, i.e., noise hits that look like real signals, to 0.42, 0.13, 0.036, 1.6×10^{-3}, and 4.0×10^{-5} per event, for settings $\alpha_{\rm w} = 3.0, 3.5, 4.0, 5.0, 6.0$, respectively. Anode / wire matching reduces the number of noise hits interpreted as signals by another factor $20/(4 \times 220)$, where ±10 samples is the region in which a second anode signal around an existing one would be missed.

Noise on wires and anodes can be considered uncorrelated, since any correlated noise does not reproduce the drift delays of true signals. The chance of picking up X/Y-matching wire noise is therefore independent of the number of steps found on the anode. Moreover, the probability of finding a wire noise hit is (almost) independent of whether a true wire signal was found, since the fraction of samples affected by signal is usually small if all wires are read out. Again we use drift time distributions to determine the noise contamination in the event samples under consideration. Fig. 22 shows the drift time distributions of events with one signal: a matching anode/wire signal, or an X/Y-matching wire signal without corresponding anode signal, or an anode signal without

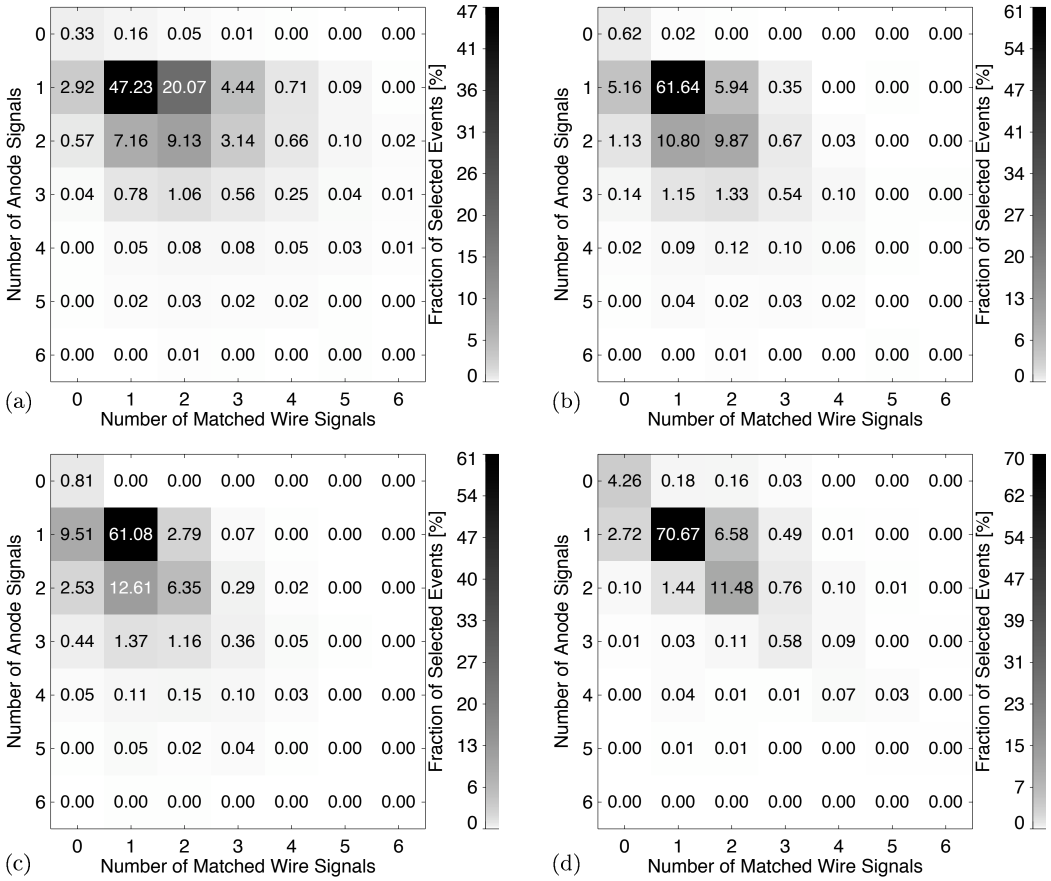

(a)

	0	1	2	3	4	5	6
0	0.33	0.16	0.05	0.01	0.00	0.00	0.00
1	2.92	47.23	20.07	4.44	0.71	0.09	0.00
2	0.57	7.16	9.13	3.14	0.66	0.10	0.02
3	0.04	0.78	1.06	0.56	0.25	0.04	0.01
4	0.00	0.05	0.08	0.08	0.05	0.03	0.01
5	0.00	0.02	0.03	0.02	0.02	0.00	0.00
6	0.00	0.00	0.01	0.00	0.00	0.00	0.00

(b)

	0	1	2	3	4	5	6
0	0.62	0.02	0.00	0.00	0.00	0.00	0.00
1	5.16	61.64	5.94	0.35	0.00	0.00	0.00
2	1.13	10.80	9.87	0.67	0.03	0.00	0.00
3	0.14	1.15	1.33	0.54	0.10	0.00	0.00
4	0.02	0.09	0.12	0.10	0.06	0.00	0.00
5	0.00	0.04	0.02	0.03	0.02	0.00	0.00
6	0.00	0.00	0.01	0.00	0.00	0.00	0.00

(c)

	0	1	2	3	4	5	6
0	0.81	0.00	0.00	0.00	0.00	0.00	0.00
1	9.51	61.08	2.79	0.07	0.00	0.00	0.00
2	2.53	12.61	6.35	0.29	0.02	0.00	0.00
3	0.44	1.37	1.16	0.36	0.05	0.00	0.00
4	0.05	0.11	0.15	0.10	0.03	0.00	0.00
5	0.00	0.05	0.02	0.04	0.00	0.00	0.00
6	0.00	0.00	0.00	0.00	0.00	0.00	0.00

(d)

	0	1	2	3	4	5	6
0	4.26	0.18	0.16	0.03	0.00	0.00	0.00
1	2.72	70.67	6.58	0.49	0.01	0.00	0.00
2	0.10	1.44	11.48	0.76	0.10	0.01	0.00
3	0.01	0.03	0.11	0.58	0.09	0.00	0.00
4	0.00	0.04	0.01	0.01	0.07	0.03	0.00
5	0.00	0.01	0.01	0.00	0.00	0.00	0.00
6	0.00	0.00	0.00	0.00	0.00	0.00	0.00

Fig. 23. Fraction of accepted events in % as a function of the number of anode signals versus the number of X/Y-matched wire signals for ^{22}Na data. (a) – (c): Anode threshold 5 and $\alpha_{\rm w} = 3.5$, 4.0, 5.0. (d): Anode threshold 8 and $\alpha_{\rm w} = 4.0$.

corresponding X/Y-matching wire signal. For the chosen range of wire and anode thresholds, wire signals in excess of those matching anode signals are due to noise, since their drift time distribution reaches beyond the maximum possible value without decline. For all true wire signals, an anode signal is found, even for high anode thresholds, through the refit procedure described in Section 3.4. These events are thus a lower limit to the noise contamination ? in the X/Y-matched wire signals, indicated as dashed line in Fig. 21. The histogram drawn with a solid line shows the ratio of events with one matching anode and (X/Y-matched) wire signal over the sum of all events with one anode signal and one or zero matching wire signals, for several anode and wire threshold settings.

Threshold settings also directly affect the ability to properly match wire signals in X and Y, and with the anode signals. Fig. 23 shows the impact of a change in wire threshold settings from low (a) to near optimum (b) to a high setting (c). The figure shows the fraction of accepted events as a function of the number of anode signals and wire signals identified, and Fig. 24 summarizes

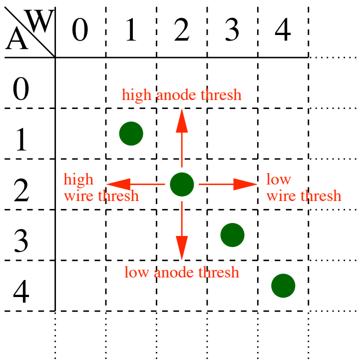

Fig. 24. The effect of anode and wire thresholds on the detection of anode ('A') and wire ('W') signals.

the dependencies on wire and anode threshold settings. If the wire threshold is set too low, too many noise hits are picked up. Even though wire hits clearly identified as noise are rejected, too many noise hits eventually end up, by chance coincidence, corresponding to the same anode. If only one is close to a true signal on that anode, the algorithm cannot determine anymore whether an additional anode signal may be overlaid, and therefore the wire signal cannot be rejected as noise. The result is an increase in off-diagonal events with more wire than anode signals. On the other side, too high wire thresholds result in an increase of wire signal misses, and therefore increase the energy threshold of the instrument by moving events in the opposite direction into the off-diagonal with less wire than anode signals. This effect is identical for both the offline wire threshold settings discussed here, and the online wire thresholds, if events are selected for the number of wire hits, and especially, if events were collected in reduced read-out mode. An analogous, but smaller, effect in the vertical direction occurs for anode threshold settings: Too high anode thresholds miss anode signals, moving events into event classes above the diagonal. However, if none of the wire signals is too close in drift time and corresponding to the same anode, all anode signals are recovered anyway in the refitting procedure, and the analysis procedure is merely slowed down. If anode thresholds are set too low, anode noise hits will move events into classes below the diagonal.

4.4 Multiplicity and confusion

Due to the high density and atomic number of LXe, the requirements on the spatial resolution of the detector for full separation of all interactions are high. As shown in previous sections, a part of the events cannot be fully resolved with the 3 mm wire pitch and the collection of charges on large anodes in the current charge-readout of the LXeTPC. Fig. 25 shows the multiplicities for γ-rays from an Y-88 source, and the result of confusion between close interac-

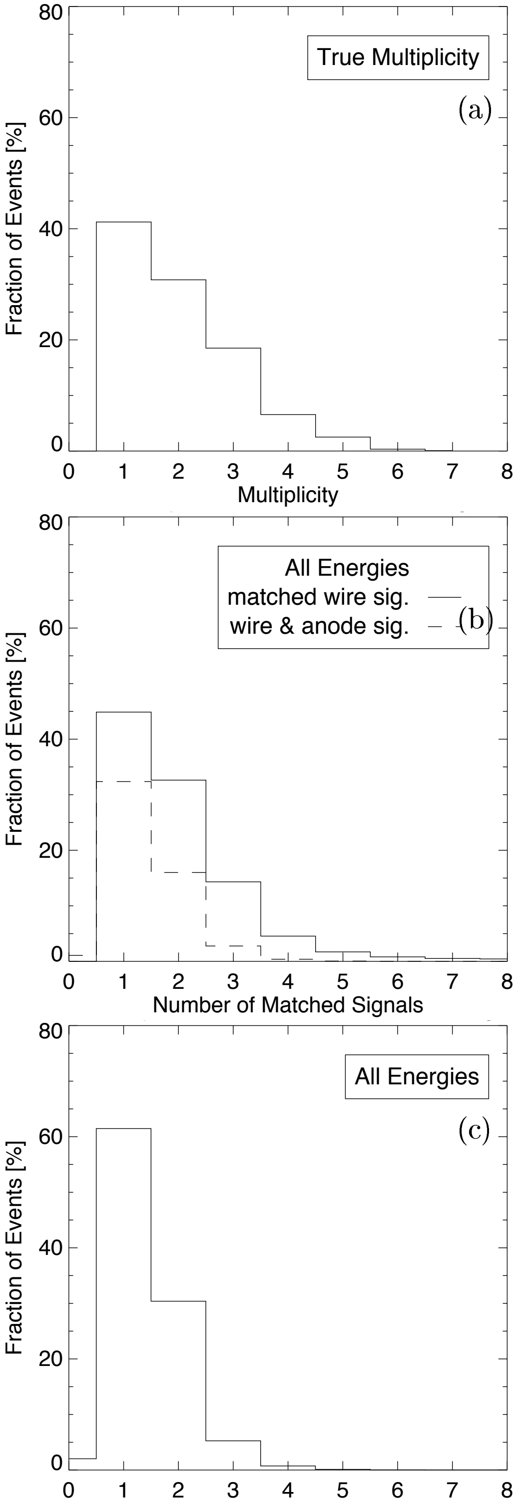

Fig. 25. Multiplicities for γ-rays from an Y-88 source (898 keV and 1836 keV) at 2 m distance on top of the chamber, with an anode threshold of $\sim$ 130 keV as only online selection. (a): True multiplicity from Monte Carlo simulation. (b): Multiplicity after X/Y wire signal matching. (c): Multiplicity after matching of wire and anode signals.

tions. The top panel shows the expectation of true multiplicity in the detector from Monte Carlo simulations with GEANT 3.21 [13,12]. The panel in the middle shows the multiplicity after X/Y-wire signal matching, which reduces the multiplicity only slightly. A more significant impact on the multiplicity is due to the matching of wire and anode signals, shown by the dashed line in the middle panel, or renormalized in the bottom panel. This has primarily to do with the inability to fit two or more steps on the same anode that are closer than about 2 μs in drift time (section 3.4). This result also points to ways of improvement in a future detector design: Firstly, a significant reduction of of the anode signal shaping before digitization would result in a rise time of the waveform given by the physical drift (about 1.25 μs for the full linear rise). This would reduce the separation limit by about a factor of 2, as the current rise time from the combination of electronic shaping and drift signal is about 2.4 μs. Secondly, the anode segmentation could be increased, or the signals could be collected directly on the second wire plane, or a strip readout. The low anode segmentation of the current set-up was aimed at simplifying the energy response of the detector, which becomes more complicated in the calibration as the segmentation increases. Collection of the charge on the second wire plane, or a strip-readout plane, would reduce the matching of signals to X/Y only, and therefore should provide best results in terms of multiplicity. Other possible draw-backs like a more complex energy calibration require further study.

5 Conclusion and Outlook

The LXeTPC centerpiece of the LXeGRIT Compton telescope has proven a powerful tool for imaging multiple gamma-ray interactions inside the detector with high spatial and moderate energy resolution. The current prototype was designed to prove this detector principle as a compact homogeneous Compton telescope, and to study the algorithms required to succesfully interpret the data. This paper demonstrates the charge signal formation in the LXeTPC as understood from field simulations and calibration data. It then summarizes a multi-year development of algorithms for signal recognition, which were gradually optimized with calibration and balloon flight data. The result is a highly stable analysis package, which distinguishes charged-particle from gamma-ray interactions, minimizes noise hits, recognizes and collects wire induction signals from multiple gamma-ray interactions, finds corresponding anode signals, and fits these for optimum spectral performance with high success rate.

The full digitization of all charge signals with flash ADC'c and memory buffers of the current data acquisition system provided the necessary base for this study, yet limited at the same time the speed with which data could be read out, transmitted, and analyzed. A future design will certainly implement many of the algorithms identified in this paper on-board, either analogue or in fast digital signal processors, so that throughput will be significantly increased, transmitted data amounts greatly reduced and the offline analysis much simplified and accelerated.

Acknowledgements

This work was supported by NASA grant NAG5-5108 to the Columbia Astrophysics Laboratory.

References

[1] E. Aprile, A. Curioni, V. Egorov, K.-L. Giboni, U. G. Oberlack, S. Ventura, T. Doke, J. Kikuchi, K. Takizawa, E. L. Chupp, P. P. Dunphy, Spectroscopy and imaging performance of the liquid xenon gamma-ray imaging telescope (LXeGRIT), in: K. A. Flanagan, O. H. W. Siegmund (Eds.), X-Ray and Gamma-Ray Instrumentation for Astronomy XI, Vol. 4140 of Proc. of SPIE, 2000, pp. 333–343, astro-ph/0012297.

[2] E. Aprile, A. Curioni, V. Egorov, K.-L. Giboni, U. G. Oberlack, S. Ventura, T. Doke, J. Kikuchi, K. Takizawa, E. L. Chupp, P. P. Dunphy, Preliminary results from the 1999 balloon flight of the liquid xenon gamma-ray imaging telescope (LXeGRIT), in: K. A. Flanagan, O. H. W. Siegmund (Eds.), X-Ray and Gamma-Ray Instrumentation for Astronomy XI, Vol. 4140 of Proc. of SPIE, 2000, pp. 344–359, astro-ph/0012398.

[3] H. Bloemen, W. Hermsen, B. N. Swanenburg, C. P. de Vries, R. Diehl, V. Schoenfelder, H. Steinle, A. W. Strong, A. Connors, M. McConnell, D. Morris, G. Stacy, K. Bennett, C. Winkler, COMPTEL imaging of the galactic disk and the separation of diffuse emission and point sources, ApJS 92 (1994) 419–423.

[4] U. Oberlack, K. Bennett, H. Bloemen, R. Diehl, C. Dupraz, W. Hermsen, J. Knödlseder, D. Morris, V. Schönfelder, A. Strong, C. Winkler, The COMPTEL 1.809 MeV all-sky image., A&AS 120 (1996) C311–C314.

[5] J. Knödlseder, D. Dixon, K. Bennett, H. Bloemen, R. Diehl, W. Hermsen, U. Oberlack, J. Ryan, V. Schönfelder, P. von Ballmoos, Image reconstruction of COMPTEL 1.8 MeV ^{26}Al line data, A&A 345 (1999) 813–825.

[6] E. Aprile, V. Egorov, K.-L. Giboni, T. Kozu, F. Xu, T. Doke, J. Kikuchi, G. J. Fishman, R. Rehage, D. Trice, The electronics read out and data acquisition system for a liquid xenon time projection chamber as balloon-borne Compton telescope, NIM A 412 (1998) 425–436.
URL http://www.astro.columbia.edu/~lxe/lxegrit

[7] E. Aprile, A. Curioni, K.-L. Giboni, U. Oberlack, S. Ventura, An upgraded data acquisition system for the balloon-borne liquid xenon gamma-ray imaging telescope LXeGRIT, IEEE Trans. Nucl. Sci. 2 (12) (2001) 185–191.
URL http://www.astro.columbia.edu/~lxe/lxegrit

[8] F. Xu, Development of a LXe-TPC Compton telescope for gamma-ray astronomy, Ph.D. thesis, Columbia University, New York, USA (Feb. 1998).

[9] R. Veenhof, Garfield, a drift-chamber simulation program, CERN, Geneva, CH, CERN Program Library entry W5050 (1997).
URL http://consult.cern.ch/writeup/garfield/main.html

[10] U. Oberlack, E. Aprile, A. Curioni, K. L. Giboni, Performance of the light trigger system in the liquid xenon gamma-ray telescope LXeGRIT, IEEE Trans. Nucl. Sci. 48 (4) (2001) 76–83.
URL http://www.astro.columbia.edu/~lxe/lxegrit

[11] E. Aprile, A. Curioni, K.-L. Giboni, M. Kobayashi, K. Ni, U. Oberlack, A new light readout system for the LXeGRIT time projection chamber, IEEE Trans. Nucl. Sci. Submitted.
URL http://www.astro.columbia.edu/~lxe/lxegrit

[12] E. Aprile, A. Curioni, K.-L. Giboni, M. Kobayashi, U. G. Oberlack, S. Ventura, E. L. Chupp, P. P. Dunphy, T. Doke, Calibration of the liquid xenon time projection chamber of the LXeGRIT compton telescope, NIM A In prep.

[13] CERN, Geneva, CH, GEANT – Detector Description and Simulation Tool, version 3.21, CERN Program Library entry W5013 (1995).
URL http://wwwinfo.cern.ch/asdoc/geant_html3/geantall.html